Iterative Multiframe Super-Resolution Algorithms for Atmospheric Turbulence-Degraded Imagery

David G. Sheppard, Bobby R. Hunt, Michael W. Marcellin

Department of Electrical and Computer Engineering, University of Arizona, Tucson, AZ 85721

Abstract

This paper is concerned with the super-resolution of atmospheric turbulence-degraded, short exposure imagery, where super-resolution refers to the removal of blur caused by a diffraction-limited optical system along with recovery of some object spatial frequency components outside the optical passband. Photon-limited space object images are of particular interest. Two strategies based on multiple exposures are explored. The first is known as deconvolution from wavefront sensing (DWFS), where estimates of the optical transfer function (OTF) associated with each exposure are derived from wavefront sensor data. New multiframe super-resolution algorithms are presented based on Bayesian maximum a posteriori (MAP) and maximum likelihood formulations. The second strategy is known as blind deconvolution, in which the OTF associated with each frame is unknown and must be estimated. A new multiframe blind deconvolution algorithm is presented based on a Bayesian maximum likelihood formulation with strict constraints incorporated using nonlinear reparameterizations. Quantitative simulation of imaging through atmospheric turbulence and wavefront sensing are used to demonstrate the super-resolution performance of the algorithms.

1. Introduction

The study of space objects (SO) such as satellites, orbital debris, and meteors is growing in importance as more platforms are sent into orbit. To avoid collisions with space objects, it is necessary to observe and catalog them using high resolution images so that their orbits can be determined and used to predict future positions. Most, if not all, SO images are acquired by ground-based optical systems observing through the earth atmosphere, and therein lies the problem. Atmospheric turbulence-induced optical distortions cause severe blurring and are an obstacle to obtaining high resolution SO images. Diffraction-limited optical systems impose resolution limitations, as well, but the atmospheric distortion is the primary resolution limiting factor for large aperture instruments. Restoration of SO imagery involves the removal of both effects.[1]

The focus of this paper is on restoration of SO imagery with *super-resolution*. Super-resolution algorithms produce a restored image in which details too fine to be resolved by the optical system are revealed, or super-resolved. Super-resolution may be defined more formally as the removal of blur caused by a diffraction-limited optical system along with meaningful recovery of object spatial frequency components outside the optical system passband.[2]

In noise, full recovery of the original object is not possible, and a solution must be defined as an element of a set of feasible solutions. Knowledge about the original scene is used to constrain the solution and reduce the size of the feasible solution set. Typical examples of such knowledge are: 1) a limited region of support in which the object of interest is smaller than the extent of the image; and 2) image positivity due the physical nature of light. The potent combination of support and positivity constraints is the basis for most super-resolution work. An important recent theoretical result in super-resolution research provides a lower bound for accurate spatial frequency recovery from this combination of constraints, where it is shown to be inversely proportional to the size of the object region of support and the noise level in the image.[2]

There are many approaches to image restoration in the literature, but not all can super-resolve. For example, linear, shift-invariant, methods such as generalized inverse filtering and optimal Wiener filtering cannot super-resolve.[2] An example of a linear, shift-variant, super-resolution algorithm is the closed form solution[3] to the Gerchberg-Papoulis algorithm,[4] also known as a projection onto convex sets (POCS) algorithm. However, most super-resolution algorithms are nonlinear and have been derived from Bayesian maximum likelihood[5–7] and maximum *a posteriori* estimates,[8,9] to name a few. For more information on super- resolution history and background, see the recent survey by Hunt.[10]

The super-resolution algorithms presented below for SO images are based on processing sequences of short exposure images. There are two reasons for so doing. First, the atmospheric turbulence distortions are not varying during image acquisition. This curbs the loss of information caused by averaging the time-varying distortion. Second, using sequences of images is an effective way to control the noise due to the low light levels in short exposure images.[11] Processing such images is difficult because most restoration techniques require knowledge of the distortions affecting each of the images in the sequence. Fortunately, this information can be gained from an auxiliary measurement using a wave front sensor (WFS) system. These systems measure the distortion of the optical wave front appearing in the telescope pupil. Restoration from WFS data is referred to as deconvolution from wave front sensing (DWFS) within the astronomical community.[12] The restoration algorithms presented below are intended to fulfill the requirement for advanced image restoration algorithms for DWFS. They are extensions of the Poisson maximum *a posteriori* algorithm[8,9] to the multiframe problem.

In the absence of WFS data, one must turn to either speckle interferometry with phase recovery or blind deconvolution. Within the astronomical community, there is growing interest in blind deconvolution, in which the distortion affecting each image is unknown and must be recovered during the deconvolution process. This may sound too good to be true, but some suprisingly good results have been presented recently.[13–15,17] The key to making these methods work is the application of *a priori* knowledge about the nature of the

degradations and the images. Using multiple differently blurred frames is in itself a powerful constraint on the restored original object image. The algorithms presented below extend the work of Conan and Thiébaut[17] to the multiframe problem and are based on Bayes maximum likelihood criteria for Poisson data.

The following sections provide an overview of the assumptions made concerning image formation through atmospheric turbulence, a survey of image restoration in atmospheric turbulence, presentation of the algorithms, and simulation results.

2. Image Formation Through Atmospheric Turbulence

A. Diffraction-Limited Image Formation

The process of image formation is central to the super-resolution problem. In this work, it is assumed that quasi-monochromatic incoherent light energy propagates from object plane sources, through an intervening medium and the telescope optical system, to an image plane. The object and image plane irradiance distributions will be denoted by $f(\xi, \eta)$ and $g(x, y)$, respectively. The medium and the optical system together constitute a mapping, denoted by the operator $L\{\cdot\}$, between the object and image spaces.

A general statement of the process is given by

$$g(x, y) = L\{f(\xi, \eta)\} \odot n(x, y) \tag{1}$$

where $\odot n(x, y)$ refers to a point by point operation with the noise process $n(x, y)$. In the absence of a disruptive medium, a rigorous expression for the operator $L\{\cdot\}$ can be derived from scalar diffraction theory. Diffraction-limited optical systems convert diverging spherical waves to spherical waves converging to a point on the image plane, or in other words, are "in focus." A linear, spatially shift-invariant, relationship exists between the object and image plane irradiance distributions.[18] The image formation process can therefore be described as

a convolution

$$g(x,y) = \int_{-\infty}^{\infty}\int_{-\infty}^{\infty} h(x-\xi, y-\eta) f(\xi,\eta) d\xi d\eta \odot n(x,y)$$
$$= (h * f)(x,y) \odot n(x,y) \quad (2)$$

where the notation $(h * f)(x,y)$ refers to the convolution of f with the optical system point spread function (PSF) h.

B. Modeling of Atmospheric Turbulence Effects

The atmosphere through which a telescope must view an object possesses a stochastic index of refraction structure which is a function of inhomogeneities in temperature and humidity. In astronomy, a distinction is commonly made between "short exposure" and "long exposure" images. During short exposure image acquisition, the turbulence structure of the atmosphere is effectively "frozen" and the image is distorted by the instantaneous turbulence structure. Such images are generally referred to as *speckle images* because of their modulated appearance. In spite of the severity of the image degradation, there is object spatial frequency information up to the diffraction limit of the telescope encoded in the image.[11,19]

The relationship between resolution and turbulence is fairly complex and can be expressed in terms of the coherence function of the wave front phase and Strehl's criterion as originally derived by Fried.[20] Fundamentally, resolution is limited by the telescope if the aperture diameter is smaller than the so-called Fried parameter r_0. And the resolution is limited by atmospheric distortion when the aperture is larger than r_0. The Fried parameter is widely used to gauge the quality of the "seeing" at any given moment. Large values of r_0 imply better seeing. A value of 10 cm is considered canonical.

Atmospheric distortion effects can be incorporated into the image formation model given by Equation (2) by defining the *generalized exit pupil function* of the telescope as the product of the distorted wave front and the telescope exit pupil function.[21] The generalized incoherent PSF can be found by applying methods from *Fourier optics*. It is important to note that

the imaging system is spatially shift-invariant only if the wave fronts from all points on the space object acquire the same distortion. The angular extent for which this is true defines that portion of the field of view referred to as the *isoplanatic patch*.[11] Super-resolution of anisoplanatic images is not addressed in this work.

3. Image Restoration in Atmospheric Turbulence

A. Classical Deconvolution

Early examples of image restoration in astronomy concern the treatment of long exposure images. The nature of the long-exposure OTF has been studied extensively and very good theoretical models have been available since the 1960's. Many of these have been used for deconvolution.[11] The short exposure OTF, on the other hand, is a realization of the stochastic phase distortion appearing across the telescope aperture and must be measured by some means. Early results from simulations of short-exposure image restoration were better than those from long-exposure images and offered support for the view that they do indeed contain more high frequency information than long exposure images. The short exposure time reduces the amount of light recorded, dictating the use of long sequences of images in order to provide robust recovery.[11]

With an estimate of the OTF, whether long or short-exposure, a number of techniques are available to perform the deconvolution. Approaches such as inverse filtering and Wiener filtering are still in use,[22] although they have lost ground to nonlinear algorithms based on maximum entropy and Bayesian estimation.[23] The Richardson-Lucy (RL) algorithm for computing the maximum likelihood estimate given Poisson image data is the method of choice for deconvolution of astronomical imagery, with entropy-based methods following close behind. The RL algorithm was discovered in the West independently by Richardson in 1972,[5] and Lucy in 1974.[6] Though the algorithm is nonlinear, it produces a photometrically linear restoration over a dynamic range of at least six stellar magnitudes. This probably explains

why it has superseded the entropy-based methods, which are known to have some problems in this regard.[26,27] Many other algorithms of note are used in the astronomical community, including projection onto convex sets (POCS) and the various CLEAN algorithms.[24,23]

B. Speckle Imaging

In 1970, A. Labeyrie published a technique called *stellar speckle interferometry* which revolutionized large telescope astronomy.[28] It was the first attempt to achieve diffraction-limited imaging with large telescopes observing through the atmosphere. In his technique, a large number of short exposure images are acquired and their power spectra are added together to form an estimate of the image power spectrum. This does not result in the loss of high spatial frequency information caused by adding together short exposure images. The expected object power spectrum can be recovered by inverse filtering. Although many factors can undermine the accuracy of the estimate in practice, speckle interferometry can provide a good estimate of the object power spectrum up to the diffraction limit of the telescope. The problem is that the phase spectrum is lost, and in general it is not possible to recover a unique image of the object.[21] Numerous methods have been proposed, of which the Knox-Thompson[29] and Bispectrum[30] methods are commonly employed.[31] The combination of speckle interferometry and phase recovery is referred to as *speckle imaging*.

C. Deconvolution from Wave Front Sensing and Adaptive Optics

Of the many significant advances in astronomical image processing since speckle interferometry, *wave front sensing (WFS) and adaptive optics* must be considered one of the most important.[32,33] In the usual configuration, the WFS system measures the wave front phase errors in the pupil of the telescope using a reference star in the isoplanatic patch. These measurements are mapped into control signals for the adaptive optics system, which changes the telescope's optical characteristics in real time. The results can be very impressive, yield-

ing nearly diffraction-limited images. When a natural reference star is not available, some systems have high-powered lasers which can provide an artificial reference star by interacting with gases in the upper atmosphere.[32,33] Post-processing of adaptive optics-compensated imagery has been proposed.[34,35]

However, building and maintaining adaptive optics systems is quite expensive and it is reasonable to seek alternatives. Moreover, it may not be feasible to retrofit an existing large telescope with adaptive optics, thus highlighting the need for a different solution in those cases. One strategy is to use a WFS to obtain estimates of the atmosphere/telescope OTF followed by post-processing for image recovery. This strategy is appealing for economic reasons but also because it may be possible to retrofit an older telescope with a WFS at reasonable cost. Another strategy, called the hybrid approach, is to build an adaptive optics system which is capable of correcting some of the turbulence-induced errors. Measurements of the residual phase error in the telescope pupil are then used for post-processing and image recovery.[12,36] Constrained nonlinear algorithms for DWFS are presented below.

D. Blind Deconvolution

The methods above rely on an estimate of the point spread function affecting the recorded image, usually from an auxiliary measurement but sometimes from a theoretical model. When such data are not available one must turn to blind deconvolution. This approach is inherently more difficult than the techniques describe above simply because one has less information. The key to the approaches reviewed below is the incorporation of a priori information. Some of the recent work in this area is summarized below.

The seminal work was published in 1968 by Oppenheim, et. al.,[37] and in 1975 by Stockham, et. al.,[38] These works were based on superposing signals in combination with homomorphic filtering. For Stockham, et. al., the problem at hand was removal of the reverberation caused by the recording horn used on old phonograph recordings. It was shown that correction of the phase distortion of a one-dimensional signal is not possible without an ensemble

of identically distorted signals. Lane and Bates[39] subsequently demonstrated that correction was possible for higher dimensional signals without ensembles. Their results showed that the Fourier transform of a K-dimensional function ($K > 1$) having compact support was zero on continuous surfaces called zero-sheets. The sheets were of dimension $2K - 2$ and resided in a space having effectively $2K$ dimensions. This information was then used to perform blind deconvolution using a single image, i.e. without using ensembles. Sensitivity to noise in the data was identified as the chief obstacle to success of the method. Others have since pursued this avenue with some success.[40,41]

Ayers and Dainty[42] spurred much of the current interest in blind deconvolution in the astronomical community. Their approach was based on projections onto convex sets (POCS). The method proved to be very promising in spite of stability problems in the presence of noise. Other researchers published improvements to the basic algorithm. For instance Davey, et al.,[43] found improvements by incorporating the Wiener filter into the iterations and using a support constraint for the object estimate. The method was improved further[44] by employing the Richardson-Lucy algorithm instead of the Wiener filter.

Other researchers began to apply constrained nonlinear estimation procedures. Holmes[45] employed the expectation maximization approach for Poisson data and arrived at dual Richardson-Lucy iterations for the object and PSF. In this formulation, positivity constraints were implicit assuming positive initial estimates. To this were added constraints on the PSF such as radial symmetry and the bandlimit associated with the diffraction-limited cutoff frequency of the optical system. Improvements to Holmes' approach were presented by Schulz.[14] Sequences of turbulence-degraded images were brought together in a maximum likelihood estimate, with penalty functions to steer the estimates away from trivial solutions. The problem of estimating the PSF was also reformulated directly in terms of the telescope pupil phase error. Using multiple frames eliminated the case where the object converged to the recorded image. Lane[46] approached the multiframe problem using data consistency with a penalty function to enforce constraints. This yielded more robust performance on simple objects than the Ayers and Dainty or Davey, et.al., algorithms. Jefferies and Christou[15,16]

improved Lane's algorithm by employing positivity, data consistency, support, band-limit, multiple image, and Fourier modulus constraints. They demonstrated super-resolution of simulated binary stars, star clusters, and relatively simple extended objects. The Lane and Jefferies and Christou approaches are characterized by their use of "soft" constraints that are not strictly enforced.

Conan and Thiébaut[17] improved upon the above by reviving Biraud's approach to strictly enforced constraints.[47] Their approach centered on a maximum likelihood formulation with reparameterization of the PSF in terms of telescope pupil phase errors. Constraints were enforced by employing nonlinear reparameterizations of the object and PSF. The algorithms presented below extend their work to the multiframe case with different constraint formulations.

4. Iterative Multiframe Super-Resolution Algorithms

In this section, iterative multiframe algorithms are derived for both deconvolution from wave front sensing and blind deconvolution. The use of multiple frames is important for controlling the noise in short-exposure images and for achieving super-resolution. Recall from the introduction that spectral recovery outside the optical passband is a function of the spatial extent of the object and the signal-to-noise ratio in the images.[2] For the blind deconvolution problem, using multiple frames has a regularizing effect on the solutions in addition to noise control.[14]

A. Derivation of Multiframe Poisson MAP Algorithms for Deconvolution from Wave Front Sensing

Given an object image f, let $\{g_k\}_{k=1}^K$ and $\{h_k\}_{k=1}^K$ be a sequence of observed images and the sequence of atmosphere/telescope PSF which correspond to them. Discrete-to-discrete image formation is assumed with the object plane indexed by coordinates i and j, and the

image plane indexed by coordinates x and y. Bayes rule provides a complete description of the conditional probabilistic relationship between the object, f, and the sequence of recorded images:

$$p\left(f, \{h_k\} | \{g_k\}\right) = \frac{p\left(\{g_k\} | f, \{h_k\}\right) p\left(f, \{h_k\}\right)}{p\left(\{g_k\}\right)}. \tag{3}$$

There are two estimates common estimates:

- the maximum likelihood (ML) estimate:

$$\hat{f} = \arg\max_{f,h} p\left(\{g_k\} | f, \{h_k\}\right), \tag{4}$$

- and the maximum a posteriori (MAP) estimate:

$$\hat{f} = \arg\max_{f,h} p\left(\{g_k\} | f, \{h_k\}\right) p\left(f, \{h_k\}\right). \tag{5}$$

A potential advantage of the MAP formulation over the ML is the inclusion of prior knowledge about the statistics of the object. In the following development, it is assumed that PSF estimates have been produced from WFS measurements. They will not be treated as statistical quantities as is possible in the general equations presented above. Assuming that the observed images are statistically independent,[1] the maximum a posteriori (MAP) estimate is given by

$$\begin{aligned} \hat{f} &= \arg\max_{f} p\left(\{g_k\} | f\right) p\left(f\right) \\ &= \arg\max_{f} p\left(f\right) \prod_k p\left(g_k | f\right) \qquad (6) \\ &= \arg\max_{f} \sum_k \ln p(g_k | f) + \ln p_f(f) \qquad (7) \end{aligned}$$

[1]It is important to note that the assumptions about statistical independence are acknowledged to be generally incorrect. They are made solely for the purpose of mathematical tractability.

after taking the natural logarithm of the right hand side of Equation (6). Solution of Equation (7) can be obtained by noting that it is sufficient to solve the system of equations

$$\sum_k \frac{\partial}{\partial f_{ij}} \left[\ln p(g_k|f)\right]\Big|_{\hat{f}} + \frac{\partial}{\partial f_{ij}} \left[\ln p(f)\right]\Big|_{\hat{f}} = 0, \tag{8}$$

By assuming Poisson emission and observation models for the object and image, respectively, one can derive the multiframe Poisson MAP algorithm given by

$$f_{ij}^{n+1} = \bar{f}_{ij}^{n} \prod_k \exp\left\{ \frac{1}{K} \left[\left(\frac{g_k}{(f^n * h_k)} - 1 \right) * h_k^+ \right]_{ij} \right\}. \tag{9}$$

where K is the number of data frames, and the notation h_k^+ refers to the adjoint of h_k ($\left(h_k^+\right)_{i,j} = (h_k)^*_{-i,-j}$). The derivation is similar to that of the single frame case[8] and will not be repeated in detail here. The object mean emission rate $\bar{f}_{ij}$ is generally unknown and implementation of Equation (9) is not possible without some additional knowledge about the object. This term can be useful for incorporating models for the object in the form of Markov random fields.[48] In the absence of such a model, it is simpler to adopt the heuristic approach that the latest estimate embodies the best knowledge about the object prior distribution. Making the substitution $\bar{f}_{ij} = f_{ij}$ yields the baseline multiframe Poisson MAP

$$f_{ij}^{n+1} = f_{ij}^{n} \prod_k \exp\left\{ \frac{1}{K} \left[\left(\frac{g_k}{(f^n * h_k)} - 1 \right) * h_k^+ \right]_{ij} \right\}. \tag{10}$$

The computational requirements of this algorithm increase linearly with the number of frames. A more efficient algorithm, referred to as the incremental version, may be derived by using the single frame PMAP algorithm with a different pair $\{g_k, h_k\}$ at each iteration. These pairs may be drawn at random from the data set or in sequence. If drawn in sequence the algorithm can be written as

$$f_{ij}^{n+1} = f_{ij}^{n} \exp\left\{ \left[\left(\frac{g_{((n))_K}}{\left(f^n * h_{((n))_K}\right)} - 1 \right) * h_{((n))_K}^+ \right]_{ij} \right\}, \tag{11}$$

where $((n))_K$ denotes the integer remainder of n divided by K. Consequently, it has the same computational requirements as the single frame version while retaining the advantages of multiple observations. The incremental and baseline versions of the algorithm offer nearly

identical super-resolution results. This suggests that the incremental algorithm is preferable in most circumstances. Appendix A shows the steps involved in the multiframe PMAP algorithms.

B. A Multiframe Maximum Likelihood Algorithm for Deconvolution from Wavefront Sensing with Strict Constraints

The multiframe maximum likelihood estimate can be reformulated as a minimization problem

$$\hat{f} = \arg\min_{f} \left[-\ln p\left(\{g_k\} | f \right) \right] \tag{12}$$

and solved by any number of numerical optimization techniques. Such methods usually require a closed form expression for the gradient, although it is possible to compute it numerically at each iteration. This algorithm is a companion to the blind deconvolution algorithm discussed later. Once again, Poisson statistics are assumed for the observed image yielding closed form expressions for the objective function and its gradient. Making the distributional substitution in Equation (12) yields

$$\begin{aligned} J(f) &= -\sum_k \sum_{x,y} \ln p\left((g_k)_{xy} \middle| f \right) \\ &\approx -\sum_k \sum_{x,y} \left((g_k)_{xy} \ln \left[(f * h_k)_{xy} \right] - (f * h_k)_{xy} \right) \end{aligned} \tag{13}$$

An expression for the gradient can be found easily

$$\frac{\partial J(f)}{\partial f_{ij}} = -\sum_k \left[\left(\frac{g_k}{(f * h_k)} - 1 \right) * h_k^+ \right]_{ij}, \tag{14}$$

and a strict positivity constraint is imposed on f_{ij} by reparameterizing it as $f_{ij} = \varphi_{ij}^2$, where φ_{ij} is free to take on any value. Enforcing constraints in this manner was proposed by Biraud,[47] and revived recently for blind deconvolution of astronomical images by Conan and Thiébaut.[17] In comparing these types of formulations with penalty functions, they found that results were significantly better using the strict formulations. This supplied the impetus

for using them in this work. One could suppose that the nonlinearity of the constraint reparameterization would make the objective function more difficult to solve because of an increase in the number of local minima. However, this was not found to be troublesome in practice. Results produced by this formulation and the multiframe Poisson MAP algorithms above were found to be nearly identical for the DWFS problem.

The components of the gradient can be found in terms of φ by applying the chain rule:

$$\begin{aligned} \frac{\partial J(f)}{\partial \varphi_{ij}} &= \frac{\partial J(f)}{\partial f_{ij}} \frac{\partial f_{ij}}{\partial \varphi_{ij}} \\ &= -2\varphi_{ij} \sum_k \left[\left(\frac{g_k}{(f * h_k)} - 1 \right) * h_k^+ \right]_{ij} . \end{aligned} \tag{15}$$

The conjugate gradient method is becoming very popular for solving inverse problems.[49] It converges much faster than gradient descent techniques or contraction mappings by employing line searching along so-called conjugate gradient directions. This avoids much of the "back-tracking" which takes place with gradient descent methods. The direction of descent at a particular iteration is a recursive function of previous search directions. For a good discussion of the details of the conjugate gradient method, see the report by Schewchuk's.[50] The Numerical Recipes conjugate gradient subroutines were used to produce the results presented here.[51] Appendix B shows the steps involved in computing the multiframe conjugate gradient maximum likelihood DWFS algorithm.

C. A Multiframe Maximum Likelihood Blind Deconvolution Algorithm with Strict Constraints

In this section, the work of Conan and Thiébaut is extended to the multiframe case and with strict bandwidth constraints for the PSF estimates. Poisson statistics are assumed for the recorded images. The objective function and object gradient components are given by Equations (13) and (15), respectively. It is necessary to compute the components of the gradient corresponding to the PSF estimates.

A three-fold reparameterization of the point spread function enforces positivity, unit

volume, and finite bandwidth simultaneously. This is given by

$$(h_k)_{ij} = \frac{(\xi * \psi_k)_{ij}^2}{\sum_{i',j'} (\xi * \psi_k)_{i'j'}^2} \tag{16}$$

where the ψ_k are the free parameters and ξ is a low pass filter designed to imposed a finite bandwidth on the PSF. The cutoff frequency of ξ should be set to half the optic cutoff frequency of the optical system because squaring the result of $\xi * \psi_k$ results in a doubling of the bandwidth. The gradient in terms of the ψ_k parameters can be found using the chain rule:

$$\begin{aligned}
\frac{\partial J(f,\{h_k\})}{\partial (\psi_k)_{ij}} &= \sum_{m,n} \frac{\partial J(f,\{h_k\})}{\partial (h_k)_{mn}} \frac{\partial (h_k)_{mn}}{\partial (\psi_k)_{ij}} \\
&= -\left(\frac{2}{\sum_{i',j'} (\xi * \psi_k)_{i'j'}^2} \right) \left[\left[\left((\xi * \psi_k) \left(\frac{g_k}{f * h_k} - 1 \right) * f^+ \right) * \xi^+ \right]_{ij} \right. \\
&\quad \left. - \left[(\xi * \psi_k) * \xi^+ \right]_{ij} \sum_{m,n} \left[\left(\frac{g_k}{f * h_k} - 1 \right) * f^+ \right]_{mn} (h_k)_{mn} \right]
\end{aligned} \tag{17}$$

where the dummy coordinates m and n index the object plane. With closed form expressions for the objective function and its gradients, the problem may be solved with any number of gradient descent-type methods. The method of conjugate gradients was also used to solve this problem. Appendix C shows the steps involved in the multiframe maximum likelihood blind deconvolution algorithm.

5. Quantitative Simulation of Imaging Through Atmospheric Turbulence and Wave Front Sensing

There are two cases of interest: 1) restoration of uncompensated images from WFS data, and 2) restoration of images by blind deconvolution. In both cases, it is necessary to simulate distortion of the optical wave front by the atmosphere and the creation of short exposure images. The former also requires simulation of the WFS system followed by translation of the WFS data into an estimate of the atmospheric phase distortion and computation of

the resulting atmosphere/telescope OTF. The methodology for quantitative simulation of imaging through turbulence and wave front sensing is presented in this section.

A. Phase Screen Generation and Image Formation

The optical wave front after passage through the atmosphere is usually modeled as a two-dimensional Gaussian random field with a Kolmogorov power spectrum, referred to as the *phase screen*.[12] A number of approaches to generating such a field exist, but the most common consists of applying an inverse Karhunen-Loeve transformation to a two-dimensional uncorrelated Gaussian random field. The KL transform matrix is derived from the Kolmogorov power spectrum using the Wiener-Kinchine theorem to compute the correlation matrix corresponding to the spectrum. This works quite well and is fairly simple to implement.[12] After generation of the phase screen, two further steps are taken. The "tilt," or linear trend, of the phase screen is removed by subtracting a plane determined by the method of least squares applied to the phase data. This results in the centering of each image. Wave front "piston" error (non-zero mean) is corrected by subtracting the mean. These basic steps are followed throughout the simulations presented below.

B. Wave Front Sensor Simulation

A Hartman WFS system measures the spatial gradient of the phase screen at an array of sampling points. The key parameters for this measurement are the number of sampling points and the accuracy of the measurements. The accuracy of the measurements is a function of the size of the subapertures in the WFS and the amount of light gathered by each subaperture. The standard deviation of the phase difference across each subaperture (normalizing by the subaperture diameter, lsa, yields the spatial phase gradient) is given by

$$\sigma = \begin{cases} \frac{0.86\pi\eta}{\sqrt{2n}} \frac{lsa}{r_0} & lsa > r_0 \\ \frac{0.74\pi\eta}{\sqrt{2n}} & lsa \leq r_0 \end{cases} \tag{18}$$

where n denotes the photon count in the subaperture, and η denotes the efficiency factor of the Hartman WFS (a value of 1.5 is assumed).[54] It is important for the subapertures to be smaller than r_0 to obtain the best accuracy. Equation (18) is used to generate simulated phase gradient measurements by introducing a normally distributed measurement error, $\varepsilon \sim N(0, \sigma^2)$. Gaussian CCD read noise was not included in the WFS simulation.

C. Translation of WFS Data

The translation of WFS phase gradient measurements into an estimate of the phase screen can be done by defining a linear transformation of the phase gradient measurements to weights in an eigenfunction expansion of the phase screen. If the phase gradient measurements for the subapertures are collected together in a column vector $\mathbf{s}$, define the linear transformation matrix $\mathbf{M}$ such that $\mathbf{c} = \mathbf{M}\mathbf{s}$ where the vector $\mathbf{c}$ contains the weights for the elementary function expansion. It is then necessary to find the matrix $\mathbf{M}$ which minimizes the squared-error

$$E = \left| \psi(u,v) - \sum_{i=1}^{N} c_i e_i(u,v) \right|^2 \tag{19}$$

where $\psi(u,v)$ is the phase function in the aperture. The general solution is given by $M = \left(H^T H\right)^{-1} H^T$ where the matrix H is a Jacobian which contains the sensitivities of the slope measurements to changes in the elementary function weights.[12] Various elementary functions could be employed here, but the Zernike polynomials were employed in this simulation. They are a set of radially symmetric, orthonormal basis functions.[55]

6. Simulation Results

The results presented in this section demonstrate the capabilities of the algorithms derived above. The HYSIM3 simulation software developed at the Air Force Institute of Technology was used to generate the test data. The parameters of the simulated speckle images were chosen to create images similar to those that would be recorded through the 1.6 m space

surveillance telescope located at the U.S. Air Force Maui Optical Station. For the simulation, each wave front sensor subaperture corresponds to a 10 cm subaperture in the telescope aperture. This provides full compensation capability for $r_0 \geq 10$ cm. Figure 1 displays the original OCNR5 satellite object image and several short-exposure images generated using the HYSIM3 code. Figure 2 displays the corresponding spectra.

All images are of 256×256 resolution and the optical cutoff of the instrument corresponds to approximately half of the folding frequency. Because the data is oversampled, no upsampling is carried out. In many practical situations, the recorded images are Nyquist-sampled or even under-sampled. In such cases, it is necessary to upsample the restorations in order to avoid aliasing caused by the super-resolution of the restored image.[8] The main simulation variables are the Fried parameter r_0 and the brightness of the space object, as measured by its visual magnitude m_v. Results are presented for $r_0 = 10$ cm. Three visual magnitudes are considered: an extremely bright object of $m_v = 0$, a moderately bright object of $m_v = 4$, and a fainter object of $m_v = 8$. These choices correspond to high, moderate, and low signal-to-noise ratio cases. Table 1 contains the expected photon counts for images acquired through the 1.6 m telescope as well those expected in each subaperture of the Hartmann sensor.

A. Multiframe Poisson MAP Results

Two versions of the multiframe PMAP algorithm were presented above: the baseline and incremental versions. From testing both of these algorithms, it was found that the results produced by the two were nearly identical in all cases. This is striking because the computational requirements are quite different. Many cases were considered and the near equivalence was uniform throughout. All of the results presented in this section for the PMAP algorithm were produced by the incremental version. Figures 3 and 4 show the Poisson MAP algorithm restorations from uncompensated images for different numbers of frames, objects with varying visual magnitudes, and for varying Fried parameter values. The algorithms were allowed to run for 1000 iterations. In many cases, this corresponds to early termination

of the algorithm's progress. Clearly, using more frames produces better restorations in all cases. The other critical factor is the brightness of the object. Super-resolution is clearly evident in the spectra of the restorations from $m_v = 0$ data and for the 50 and 200 frame restorations from $m_v = 4$ data. For fainter objects, more frames are required to maintain the quality of the restoration. The restorations from $m_v = 8$ data demonstrate that the algorithms are near the lower limits of acceptable performance and that 200 frames are required to obtain a reasonable restoration. Both the SNR of the data and the worsening performance of the WFS system are contributing factors in the decline of performance with decreasing object brightness. The original object image or its spectrum is included in all of the images for direct comparison.

The best presentation of the restoration results seems to be the restored image with a range-compressed Fourier transform magnitude image. Other possibilities include the family of one-dimensional curves comparing the restored image with the original in terms of phase error, SNR, correlation, or covariance versus radial distance from $(f_x, f_y) = (0, 0)$. However, the super-resolution details evident in the two-dimensional range-compressed spectra get lost in the data reduction process.

B. Multiframe Maximum Likelihood DWFS With Strict Constraints

After 40 iterations of the nonlinear conjugate gradient method, the similarity to the output from the PMAP algorithms is striking. This is not too surprising in view of the prior work in which Bayesian algorithms are shown to be related to minimum cross-entropy algorithms under certain distributional assumptions, i.e. Poisson data.[52] Due to the similarity of these results to those for PMAP, imagery is not included here for this method. The conjugate gradient technique offers a considerable acceleration of the computation in terms of iterations, although total program execution time is on par with that of the baseline PMAP because of the line search at each iteration. A parallelized version of algorithm was also implemented on the parallel IBM SP2.

C. Multiframe Maximum Likelihood Blind Deconvolution with Strict Constraints

Figures 5 and 6 display sample output from the multiframe maximum likelihood blind deconvolution algorithm for a visual magnitude $m_v = 4$ OCNR5 satellite object. Recall that strict constraints are employed for positivity on the object and strict positivity, unit volume, and bandwidth constraints on the PSF estimates. As expected, the results from the blind algorithm are not as free of artifacts as the DWFS results. Many algorithms in the literature do not perform well on extended objects. In light of this, the results are encouraging. Super- resolution is in evidence, although not to the same degree as in the DWFS results. An interesting subject for further study is to determine if a crossover exists for which the blind algorithm would outperform the DFWS approaches with images acquired through a larger aperture. Also, an explicit support constraint was not used. Such a constraint would improve the results even further. The algorithm was implemented in C code on the parallel IBM SP2 using the Message Passing Interface (MPI) in order to make the execution time manageable.

7. Conclusion

New multiframe algorithms for constrained nonlinear deconvolution from wave front sensing and blind deconvolution were presented above. Additionally, super-resolution of extended space object images was demonstrated in both the DWFS and blind cases using careful simulation of imaging through atmospheric turbulence. The use of multiple frames in the design of the algorithms was instrumental in controlling the noise present in photon-limited images and for regularizing the blind deconvolution process. The results indicate that post-processing of uncompensated images may be a viable alternative to building fully compensated adaptive optics systems. Retrofitting existing large telescopes with wave front sensor systems may also be the most effective way of bringing them into the modern era of image recovery. It should be stressed that when real time image recovery is critical, the approaches

presented above do not provide a viable alternative to adaptive optics.

The results produced by blind deconvolution were not as good as those from wave front sensing, which is not surprising given the inherent difficulty of the problem. However, they demonstrate that good image recovery is possible in this mode of operation for extended satellite objects. It may be that a crossover point exists for which blind deconvolution would outperform other techniques given images acquired from a larger instrument. These and other questions will be addressed in future work.

Acknowledgments

The authors wish to express their appreciation to Dr. Michael Roggeman for providing the HYSIM3 software and for helpful advice regarding wave front sensing simulation. This research was supported by the U.S. Air Force under contract number SC-92C-04-31.

Appendix A: Steps involved in the multiframe PMAP DWFS algorithms

1. $n = 0$

2. Compute initial estimate:

   $f^0 = \frac{1}{K} \sum_{k=1}^{K} g_k$

   (positivity should be imposed on the elements of f^0)

3. $$\begin{cases} f_{ij}^{n+1} = f_{ij}^n \prod_k \exp\left\{ \frac{1}{K} \left[\left(\frac{g_k}{(f^n * h_k)} - 1 \right) * h_k^+ \right]_{ij} \right\}, & \text{(Baseline)} \\ f_{ij}^{n+1} = f_{ij}^n \exp\left\{ \left[\left(\frac{g_{((n))_K}}{\left(f * h_{((n))_K}\right)} - 1 \right) * h_{((n))_K}^+ \right]_{ij} \right\}, & \text{(Incremental)} \end{cases}$$

4. $n = n + 1$

5. if $n = n_{max}$, stop

6. apply a suitable stopping criterion, i.e., if $\frac{\|f^{n+1} - f^n\|}{\|f^n\|} < \varepsilon$, stop; else repeat step 3

Appendix B: Steps involved in the multiframe conjugate gradient DWFS algorithm

Equations for objective function J and it's gradients

- $J\left(\varphi^n\right) = -\sum_k \sum_{x,y} \left(\left(g_k\right)_{xy} \ln \left[\left(\left(\varphi^n\right)^2 * h_k \right)_{xy} \right] - \left(\left(\varphi^n\right)^2 * h_k \right)_{xy} \right)$
- $J^{'}\left(\varphi^n\right)\big|_{ij} = \frac{\partial J(f^n)}{\partial \varphi^n_{ij}} = \frac{\partial J(f^n)}{\partial f^n_{ij}} \frac{\partial f^n_{ij}}{\partial \varphi^n_{ij}} = -2\varphi^n_{ij} \sum_k \left[\left(\frac{g_k}{\left((\varphi^n)^2 * h_k \right)} - 1 \right) * h^+_k \right]_{ij}$

where the notation $J^{'}\left(\varphi^n\right)$ refers to the lexicographically stacked vector of gradient values

Outline of Nonlinear CG method

1. Initialization

   $n = 0$

   $\varphi^n = \sqrt{f^n} = \sqrt{\frac{1}{K} \sum_{k=1}^{K} g_k}$

   $d^n = r^n = -J^{'}\left(\varphi^n\right)$

2. Line search

   find α^n that minimizes $J\left(\varphi^n + \alpha^n d^n\right)$ using the Secant method

3. Compute new estimate

   $\varphi^{n+1} = \varphi^n + \alpha^n d^n$

4. Compute new conjugate gradient direction

   $r^{n+1} = -J^{'}\left(\varphi^{n+1}\right)$ $\beta^{n+1} = \max\left\{ \frac{\left(r^{n+1}\right)^T \left(r^{n+1} - r^n\right)}{\left(r^n\right)^T r^n}, 0 \right\}$, the Polak-Ribiere form

   $d^{n+1} = r^{n+1} + \beta^{n+1} d^n$

5. $n = n + 1$

6. if $n = n_{max}$, then stop, else repeat step 2

Appendix C: Steps involved in the multiframe conjugate gradient blind deconvolution algorithm

Equations for objective function J and it's gradients

- $J\left(\varphi^n, \psi_1^n, \ldots, \psi_K^n\right) = -\sum_k \sum_{x,y} \left((g_k)_{xy} \ln \left[\left((\varphi^n)^2 * \frac{\left(\xi * \psi_k^n\right)^2}{\sum_{i',j'} \left(\xi * \psi_k^n\right)^2_{i'j'}} \right)_{xy} \right] - \left((\varphi^n)^2 * \frac{\left(\xi * \psi_k^n\right)^2}{\sum_{i',j'} \left(\xi * \psi_k^n\right)^2_{i'j'}} \right)_{xy} \right)$
- $J'\left(\varphi^n\right)\big|_{ij} = \frac{\partial J(f^n)}{\partial \varphi_{ij}^n} = \frac{\partial J(f^n)}{\partial f_{ij}^n} \frac{\partial f_{ij}^n}{\partial \varphi_{ij}^n} = -2\varphi_{ij}^n \sum_k \left[\left(\frac{g_k}{\left((\varphi^n)^2 * h_k\right)} - 1 \right) * h_k^+ \right]_{ij}$
- $J'\left(\psi_k^n\right)\big|_{ij} = \frac{\partial J(f, \{h_k\})}{\partial (\psi_k)_{ij}} = -\left(\frac{2}{\sum_{i',j'} (\xi * \psi_k)^2_{i'j'}} \right) \left[\left[\left((\xi * \psi_k) \left(\frac{g_k}{f * h_k} - 1 \right) * f^+ \right) * \xi^+ \right]_{ij} - \left[(\xi * \psi_k) * \xi^+ \right]_{ij} \sum_{mn} \left[\left(\frac{g_k}{f * h_k} - 1 \right) * f^+ \right]_{mn} (h_k)_{mn} \right]$

where the notation $J'\left(\varphi^n : \psi_1^n : \ldots : \psi_K^n\right)$ refers to the lexicographically stacked vector of gradient values

Outline of Nonlinear CG method

1. Initialization

   $n = 0$

   $\varphi^n = \sqrt{f^n} = \sqrt{\frac{1}{K} \sum_{k=1}^K g_k}$

   $\psi_k^n = \sqrt{h_k^n}$ where the h_k^n are initially wide Gaussians

   $d^n = r^n = -J'\left(\varphi^n : \psi_1^n : \ldots : \psi_K^n\right)$

2. Line search

   Find α^n that minimizes $J\left([\varphi^n : \psi_1^n : \ldots : \psi_K^n] + \alpha^n d^n\right)$ using the Secant method

3. Compute new estimate

   $\left[\varphi^{n+1} : \psi_1^{n+1} : \ldots : \psi_K^{n+1}\right] = [\varphi^n : \psi_1^n : \ldots : \psi_K^n] + \alpha^n d^n$

4. Compute new conjugate gradient direction

   $r^{n+1} = -J'\left(\varphi^{n+1} : \psi_1^{n+1} : \ldots : \psi_K^{n+1}\right)$

   $\beta^{n+1} = \max\left\{\frac{\left(r^{n+1}\right)^T\left(r^{n+1}-r^n\right)}{\left(r^n\right)^T r^n}, 0\right\}$, the Polak-Ribiere form

   $d^{n+1} = r^{n+1} + \beta^{n+1} d^n$

5. $n = n + 1$

6. if $n = n_{max}$, then stop, else repeat step 2

REFERENCES

1. H. C. Andrews and B. R. Hunt, *Digital Image Restoration* (Prentice-Hall: Englewood Cliffs, NJ), 1977.

2. P. J. Sementilli, B. R. Hunt, and M. S. Nadar, "Analysis of the limit to super-resolution in incoherent imaging," *J. Opt. Soc. Am. A*, vol. 10, no. 11, Nov. 1993, 2265–76.

3. D. O. Walsh, P. A. Delaney, and M. W. Marcellin, "Non-iterative implementation of a class of iterative signal restoration algorithms," *Proc. Intl. Conf. Acoustics, Speech, & Signal Proc., Atlanta, GA, USA*, 7-10 May 1996, 1672-75.

4. R. W. Gerchberg, "Super-resolution through error energy reduction," *Opt. Acta*, vol. 21, no. 9, Sep. 1974, 709–20.

5. W. H. Richardson, "Bayesian-based iterative method of image restoration," J. Opt. Soc. Am. A, Vol. 62, No. 1, Jan. 1972, 55-59.

6. L. B. Lucy, "An iterative technique for the rectification of observed distributions," Astron. J., vol. 79, no. 6, June 1974, 745-59.

7. T. J. Holmes, "Maximum likelihood image restoration adapted for noncoherent imaging," *J. Opt. Soc. Am. A*, vol. 5, no. 5, May 1988, 666–73.

8. B. R. Hunt and P. J. Sementilli, "Description of a Poisson imagery super-resolution algorithm," in *Astronomical Data Analysis Software and Systems I*, D. Worral, C. Biemesderfer and J. Barnes, eds. (Astronomy Society of the Pacific: San Francisco), 1992, 196-99.

9. E. S. Meinel, "Origins of linear and nonlinear recursive restoration algorithms," *J. Opt. Soc. Am. A*, vol. 3, no. 6, June 1986, 787-99.

10. B. R. Hunt, "Super-resolution of images: algorithms, principles, performance," *Int. J. Imaging Sys. and Tech.*, vol. 6, winter 1995, 297–304.

11. F. Roddier, "The effects of atmospheric turbulence in optical astronomy," in *Progress in Optics XIX*, E. Wolf, ed. (North-Holland, Amsterdam, Netherlands), 1981, 281-376.

12. M. C. Roggeman and B. Welsh, *Imaging Through Turbulence* (CRC Press: New York, NY), 1996.

13. D. Kundur and D. Hatzinakos, "Blind image deconvolution," *IEEE Signal Proc. Mag.*, vol. 13, no. 3, May 1996, 43-64.

14. T. J. Schulz, "Multiframe blind deconvolution of astronomical images," *J. Opt. Soc. Am. A,* vol. 10, no. 5, May 1993, 1064-73.

15. S. M. Jefferies and J. C. Christou, "Restoration of astronomical images by iterative blind deconvolution," *Astrophys. J.*, vol. 415, no. 2, 1 Oct. 1993, 862-74.

16. J. C. Christou, E. K. Hege, and S. M. Jefferies, "Speckle deconvolution imaging using an iterative algorithm," *Proceedings SPIE*, vol. 2566 (1995), 134-43.

17. E. Thiébaut and J.-M Conan, "Strict a priori constraints for maximum-likelihood blind deconvolution," *J. Opt. Soc. Am. A,* vol. 12, no. 3, Mar. 1995, 485-92.

18. J. W. Goodman, *Introduction to Fourier Optics* (McGraw-Hill: New York, NY), 1968.

19. R. R. Beland, "Propagation through atmospheric optical turbulence," *The Infrared & Electro-Optical Handbook, Vol. 2, Atmospheric Propagation of Radiation*, F. G. Smith, ed. (SPIE Optical Engineering Press: Bellingham, WA), 1993, 157-232.

20. D. L. Fried, "Optical resolution through a randomly inhomogeneous medium for very long and very short exposures," *J. Opt. Soc. Am. A*, vol. 56, no. 10, Oct. 1966, 1372-79.

21. J. C. Dainty, "Stellar speckle interferometry", in *Laser Speckle and Related Phenomena, 2nd Ed.*, J. C. Dainty, ed. (Springer-Verlag: Berlin, Germany), 1983, 256-320.

22. P. A. Jansson, "Traditional linear deconvolution methods," in *Deconvolution of Images and Spectra*, P. A. Jansson, Ed. (Academic Press: New York, NY), 1997.

23. P. A. Jansson, "Modern constrained nonlinear methods," in *Deconvolution of Images and Spectra*, P. A. Jansson, Ed. (Academic Press: New York, NY), 1997.

24. H.-M. Adorf, "Hubble Space Telescope image restoration in its fourth year," *Inverse Problems,* vol. 11, no. 4, Aug. 1995, 639-53.

25. H.-M. Adorf, R. N. Hook, and L. B. Lucy, "HST image restoration developments at the ST-ECF," *Int. J. Imaging Sys. and Tech.*, vol. 6, winter 1995, 339-49.

26. R. J. Hanisch and R. L. White, "HST image restoration: current capabilities and future prospects," in *Very High Angular Resolution Imaging*, J. G. Robertson and W. J. Tango, eds. (Kluwer: Dordrecht, Germany), 1994, 61-9.

27. R. J. Hanisch, R. L. White and R. L Gilliland, "Deconvolution of Hubble Space Telescope images and spectra," in *Deconvolution of Images and Spectra*, P. A. Jansson, Ed. (Academic Press: New York, NY), 1997.

28. A. Labeyrie, "Attainment of diffraction-limited resolution in large telescopes by Fourier analysing speckle patterns in star images," *Astron. & Astrophys.*, vol. 6, no. 1, May 1970, 85-7.

29. K. T. Knox and B. J. Thompson, "Recovery of images from atmospherically degraded short exposure images," *Astrophys. J.*, vol. 193, 1974, L45-48.

30. A. W. Lohman, G. Weigelt, and B. Wirnitzer, "Speckle masking in astronomy: triple correlation theory and applications," *Appl. Opt.*, vol. 22, 1983, 4028-37.

31. G. R. Ayers, M. J. Northcott, and J. C. Dainty, "Knox-Thompson and triple correlation imaging through atmospheric turbulence," *J. Opt. Soc. Am. A*, vol. 5, 1988, 963-985.

32. L. A. Thompson, "Adaptive optics in astronomy," *Physics Today*, vol. 47, no. 12, Dec. 1994, 24-31.

33. T. E. Bell, "Electronics and the stars," *IEEE Spectrum*, vol. 32, no. 8, Aug. 1995, 16-24.

34. J. C. Christou, "Blind deconvolution post-processing of images corrected by adaptive optics," *Proceedings SPIE*, vol. 2534 (1995), 226-34.

35. E. K. Hege, J. R. P. Angel, M. Cheselka, and M. Lloyd-Hart, "Simulation of aperture synthesis with the Large Binocular Telescope," *Proceedings SPIE*, vol. 2566 (1995), 144-55.

36. J.-M. Conan, V. Michau, and G. Rousset, "Signal-to-noise ratio and bias of various deconvolution from wavefront sensing estimators," *Proceedings SPIE*, vol. 2828 (1996), 332-39.

37. A. V. Oppenheim, R. W. Schafer, and T. G. Stockham, "Nonlinear filtering of multiplied and convolved signals," *Proc. IEEE*, vol. 56, no. 8, 1968, 1264-91.

38. T. G. Stockham, Jr., T. M. Cannon, R. B. Ingebretsen, "Blind deconvolution through digital signal processing," *Proc. IEEE*, vol. 63, no. 4, Apr. 1975, 678-92.

39. R. G. Lane and R. H. T. Bates, "Automatic multidimensional deconvolution," *J. Opt. Soc. Am. A,* vol. 4, no. 1, Jan. 1987, 180-88.

40. B. L. Satherly and P. J. Bones, "Zero tracks for blind deconvolution of blurred ensembles," *Applied Optics*, vol. 33, no. 11, Apr. 1994, 2197-205.

41. P. J. Bones, C. R. Parker, B. L. Satherly, and R. W. Watson, "Deconvolution and phase retrieval with use of zero sheets," *J. Opt. Soc. Am. A*, vol. 12, no. 9, Sep. 1995, 1842-57

42. G. R. Ayers and J. C. Dainty, "Iterative blind deconvolution method and its applications," *Optics Letters*, vol. 13, no. 7, Jul. 1988, 547-9.

43. B. L. K. Davey, R. G. Lane and R. H. T. Bates, "Blind deconvolution of noisy complex-valued image," *Optics Comm.*, Vol. 69, No. 5,6, 15 Jan. 1989, 353-6.

44. F. Tsumuraya, N. Miura, and N. Baba, "Iterative blind deconvolution method using Lucy's algorithm," *Astron. Astrophys.*, vol. 282, no. 2, Feb. 1994, 699-708.

45. T. J. Holmes, "Blind deconvolution of quantum-limited incoherent imagery: maximum-likelihood approach," *J. Opt. Soc. Am. A,* vol. 9, no. 7, July 1992, 1052-61.

46. R. G. Lane, "Blind deconvolution of speckle images," *J. Opt. Soc. Am. A,* vol. 9, no. 9, Sep. 1992, 1508-14.

47. Y. Biraud, "A new approach for increasing the resolving power by data processing," *Astron. & Astrophys.*, vol. 1, no. 1, Jan. 1969, 124-7.

48. P. J. Sementilli, "Suppression of artifacts in super-resolved images," Ph.D. Dissertation, University of Arizona, Tucson 1993.

49. M. Hanke, *Conjugate Gradient Type Methods for Ill-Posed Problems* (John Wiley & Sons: New York, NY), 1995.

50. J. R. Shewchuk, "An introduction to the conjugate gradient method without the agonizing pain," Technical Report CMU-CS-94-125, Carnegie Mellon University, School of Computer Science, Pittsburgh, Mar. 1994.

51. W. H. Press, B. P. Flannery, S. A. Teukolsky, and W. T. Vetterling, *Numerical Recipes in C* (Cambridge University Press: Cambridge, MA), 1988

52. M. S. Nadar, "Minimum cross-entropy formulations in image super-resolution," Ph.D. Dissertation, University of Arizona, Tucson, 1996.

53. B. R. Frieden, *Probability, Statistical Optics, and Data Testing* (Springer-Verlag: New York, NY), 1991.

54. M. C. Roggeman, B. L. Ellerbroek, and T. A. Rhoadarmer, "Widening the effective field of view of adaptive-optics telescopes by deconvolution from wave-front sensing: average and signal-to-noise ratio performance," *Applied Optics*, vol. 34, no. 8, Mar. 1995, 1432-44.

55. R. J. Noll, "Zernike polynomials and atmospheric turbulence," *J. Opt. Soc. Am. A*, vol.

66, no. 3, Mar. 1966, 207-11.

TABLES

Table 1. Expected image and subaperture photon counts as a function of object visual magnitude (1.6 m telescope with 10 cm subaps.).

$\mathbf{m}_v$	**Photons/Image**	**Photons/Subaperture**
0	65,590,000	600,300
4	1,648,000	15,083
8	41,390	378

FIGURES

Fig. 1. Original OCNR5 satellite object and sample tilt-corrected simulated short-exposure images for different visual magnitudes m_v ($r_0 = 10$ cm). Clockwise from upper left: OCNR5 object, $m_v = 0$ frame, $m_v = 4$ frame, $m_v = 8$ frame.

Fig. 2. Spectra of images from Fig. 1. Clockwise from upper left: OCNR5 object spectrum, $m_v = 0$ frame spectrum, $m_v = 4$ frame spectrum, $m_v = 8$ frame spectrum. All spectra are range compressed using $\log_{10}(1 + |\cdot|^2)$.

Fig. 3. Restoration of a simulated OCNR5 satellite object of visual magnitude $m_v = 4$ using the multiframe incremental Poisson MAP algorithm with varying number of frames ($r_0 = 10$ cm). Clockwise from upper left: OCNR5 object, 10 frame restoration, 50 frame restoration, 200 frame restoration.

Fig. 4. Spectra of images from Fig. 3. Clockwise from upper left: OCNR5 object spectrum, 10 frame restoration spectrum, 50 restoration spectrum, 200 restoration spectrum. All spectra are range compressed using $\log_{10}(1 + |\cdot|^2)$.

Fig. 5. Restoration of a simulated OCNR5 satellite object of visual magnitude $m_v = 4$ using the multiframe maximum likelihood blind deconvolution algorithm with varying number of frames ($r_0 = 10$ cm). Clockwise from upper left: OCNR5 object, 10 frame restoration, 50 frames restoration, 200 frames restoration.

Fig. 6. Spectra of images from Fig. 5. Clockwise from upper left: OCNR5 object spectrum, 10 frame restoration spectrum, 50 restoration spectrum, 200 restoration spectrum. All spectra are range compressed using $\log_{10}(1 + |\cdot|^2)$.

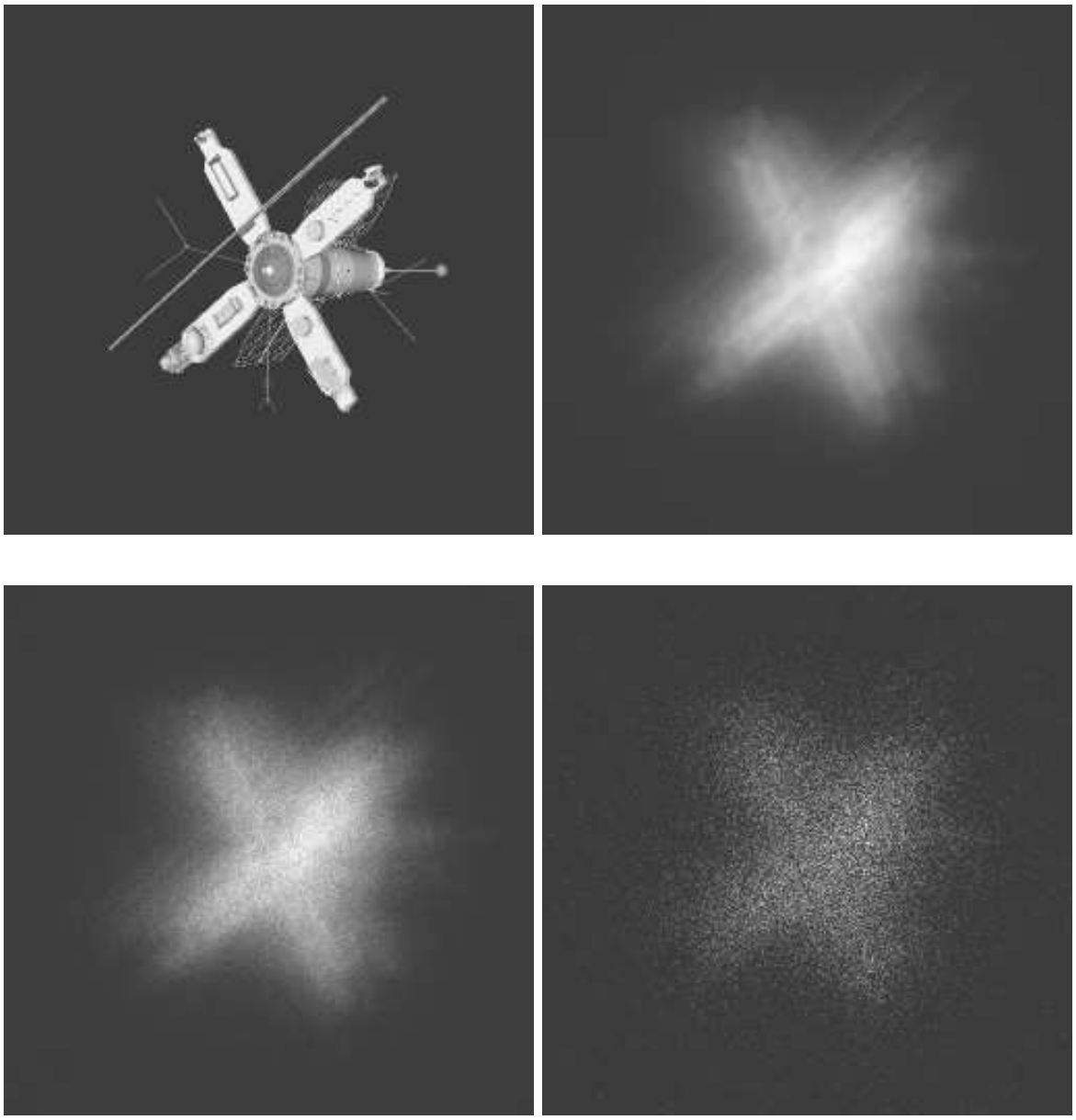

Fig. 1.

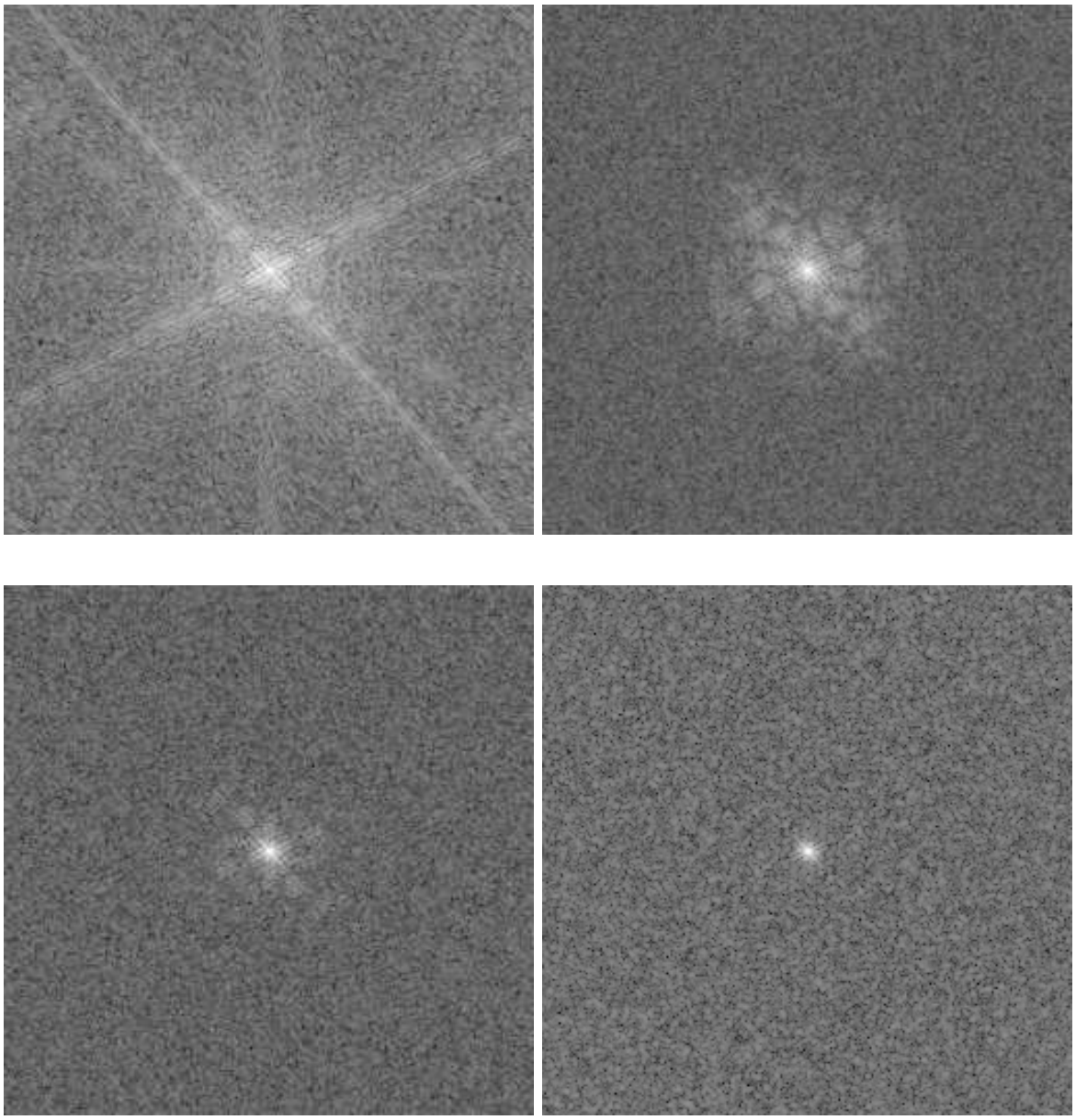

Fig. 2.

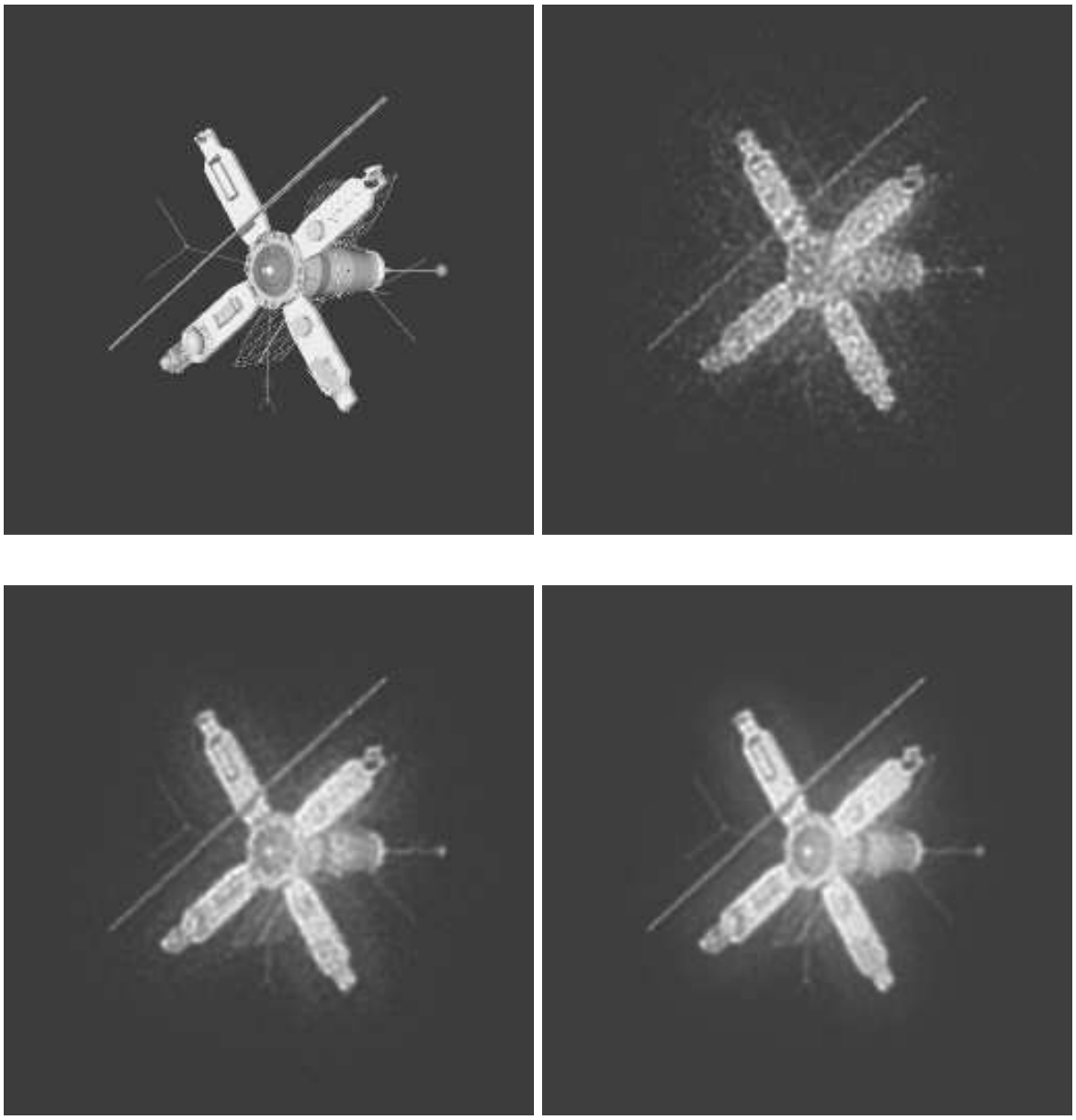

Fig. 3.

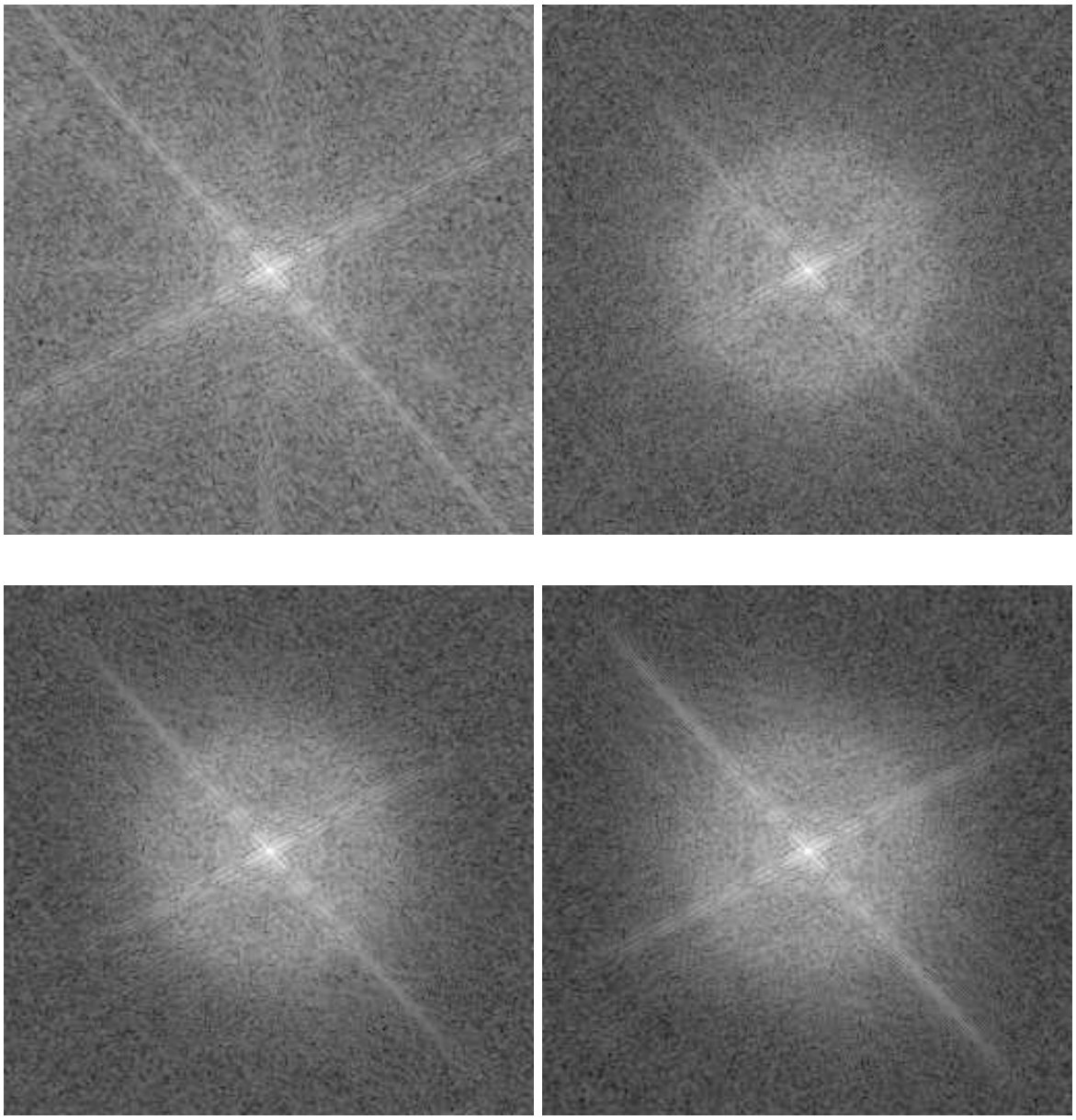

Fig. 4.

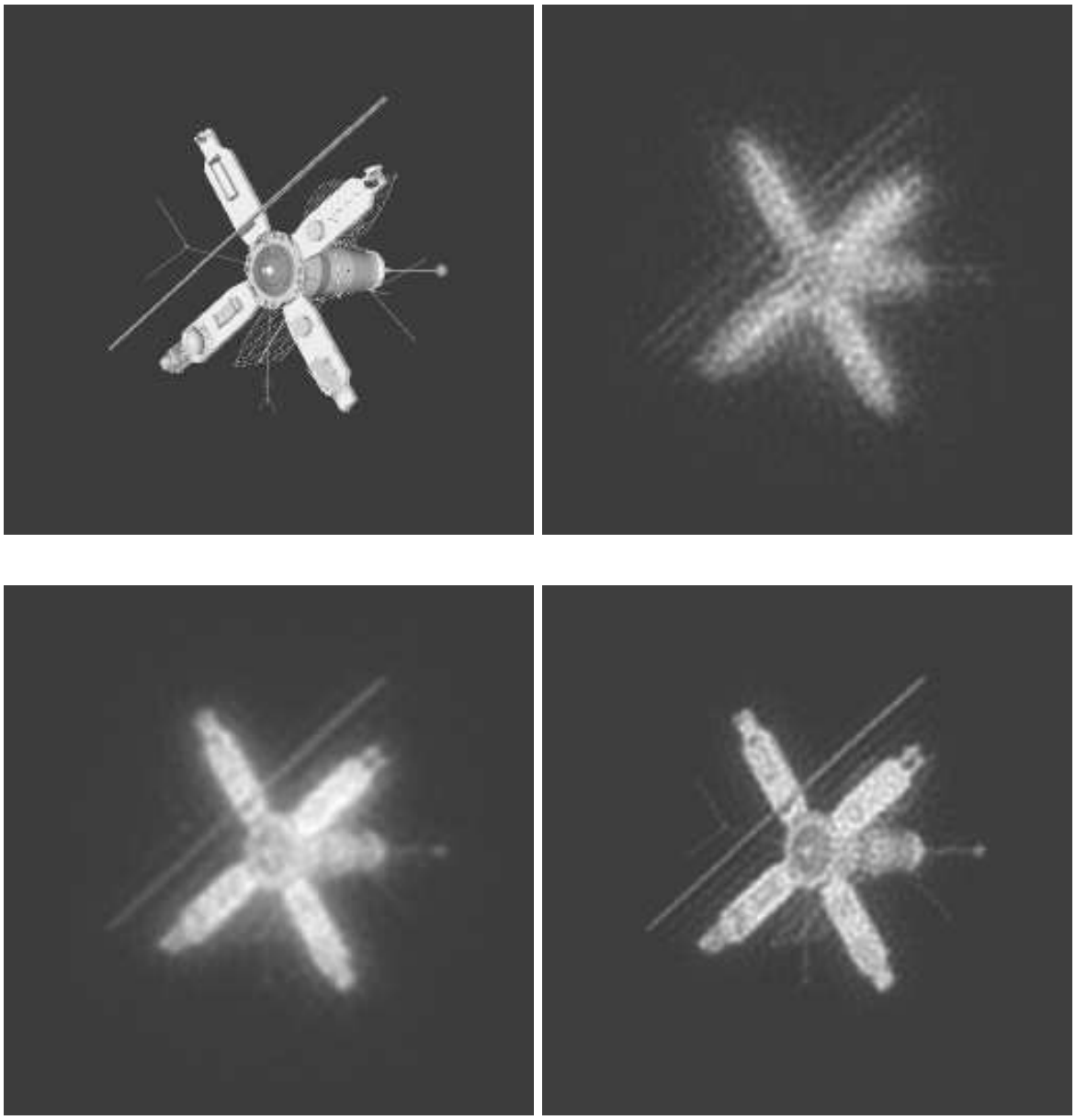

Fig. 5.

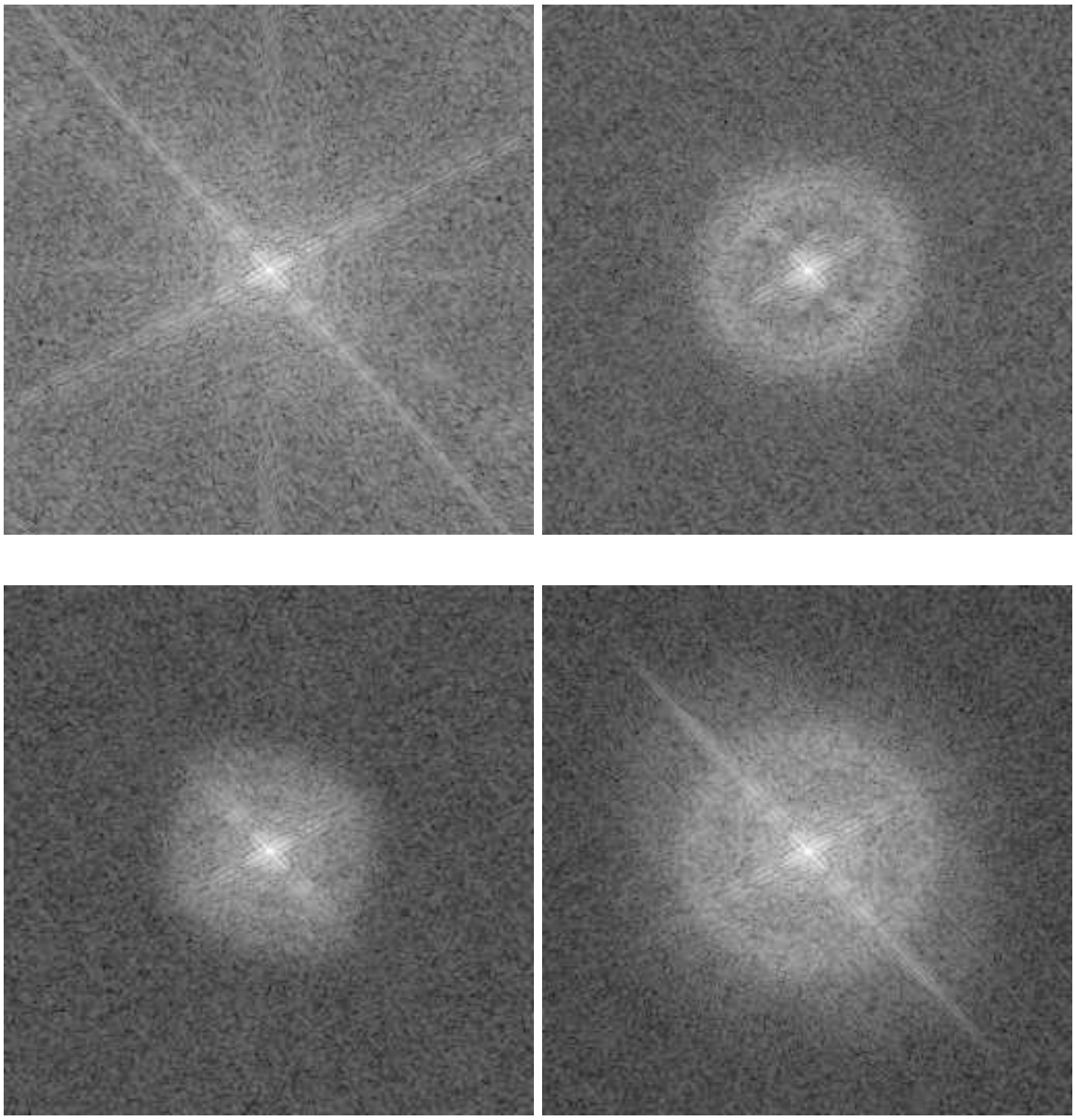

Fig. 6.